3D Human Airway Segmentation for Virtual Bronchoscopy

A.P. Kiraly,[1] W.E. Higgins,[1,2] E.A. Hoffman,[2] G. McLennan,[2] and J. M. Reinhardt[3]

[1]Department of Computer Science and Engineering

Penn State University, University Park, PA 16802 USA

[2]College of Medicine, University of Iowa, Iowa City, IA 52242 USA

[3]College of Engineering, University of Iowa, Iowa City, IA 52242 USA

ABSTRACT

This paper describes a new airway segmentation algorithm that improves the speed of morphological-based segmentation approaches. Airway segmentation methods based on morphological operators suffer from the indiscriminant application of all operators to a large area. Using the results of three-dimensional (3D) region growing, the discrete application of larger operators is possible. This change can greatly decrease the execution time of the algorithm. This hybrid approach typically runs 5 to 10 times faster than the original algorithm. 3D adaptive region growing, morphological segmentation, and the hybrid approach are then compared via data obtained from human volunteers using a Marconi MX8000 scanner with the lungs held at 85% TLC. Results show that filtering improves robustness of these techniques. The hybrid approach allows for the practical use of morphological operators to create a clinically useful segmentation. We also demonstrate the method's utility for peripheral nodule analysis in a human case.

Keywords: pulmonary, X-ray CT, airways, segmentation, virtual bronchoscopy, virtual endoscopy, peripheral nodules

1. INTRODUCTION

New multidetector helical CT scanners can produce three-dimensional (3D) volumetric images of the human airway tree consisting of hundreds of two-dimensional (2D) sections.[1] A typical 3D image can consist of 400 512×512 0.6 mm sections. Such images provide an excellent basis for virtual bronchoscopy (VB) applications[2–11] and for general airway analysis.[12,7,13,14] These applications require segmentation of the airway tree before further analysis can continue. Manual interactive segmentation has been applied in some cases, but routine manual analysis is impractical for the large 3D images arising from the new scanners.[15,16] A variety of semi-automatic airway segmentation techniques have been proposed, but none have been conclusively proven to be adequate for very large high-resolution 3D CT chest images.[17,18,15,3,19–24,16,14]

We present a new method for 3D airway segmentation that combines region growing and mathematical morphology operations. This hybrid method gives results equivalent to a previously proposed morphology-only approach,[16] but greatly reduces the computer execution time. An important part of this paper is a comparison study of the method against two other competing 3D airway-tree segmentation methods. This study reveals that mild image filtering can greatly increase the robustness of the methods in the case of patient breathing artifacts, stent distortion, and partial volume artifacts. We finally illustrate the utility of 3D airway segmentation to a VB-assisted mediastinal lymph-node biopsy. The remainder of this section reviews the airway segmentation problem and previously proposed segmentation methods.

A 3D CT image of the chest, I, is comprised of a stack of Z_{size} contiguous slices. Each slice consists of $X_{size} \times Y_{size}$ voxels (typically 512×512). Each voxel (x, y, z) has intensity value $I(x, y, z)$ and spacing $(\Delta x, \Delta y, \Delta z)$. The human airway tree as depicted in a 3D image consists of a set of connected, dark, branching tubular structures that tend to decrease in diameter as the branching progresses. CT images are reasonably well calibrated such that air is at about -1000 Hounsfield Units (HU) (i.e., $I(x, y, z)$ = -1000 for a pure air voxel (x, y, z)) while water is at 0 HU.[15] Soft tissues, such as those in the mediastinum, are situated in the range of -100 HU to 200 HU, and bone appears at +1000 HU.[25]

Airway-tree segmentation is a challenging problem for several reasons. While airway voxels are generally near -1000 HU, noise and partial volume effects make it impossible to use a simple threshold to identify all airway voxels

Send correspondence to JMR; email: joe-reinhardt@uiowa.edu

within an image.[26] Whenever mixtures of different tissue types comprise a voxel, intermediate gray-level values result.[27] Voxels straddling air and airway walls typically have values well above -1000 HU. Resolving these partial voxels into tissues components can be done through statistical methods.[27–30] Also, due to the size of the voxel, thin or stenosed airways can appear broken or discontinuous. Finally, image reconstruction artifacts, such as using a sharp high-frequency kernel, can result discontinuous-appearing airways.[25] Such discontinuities can result in parenchymal leakage and over segmentation.

Previously proposed airway segmentation methods have employed four strategies:

1. Knowledge-based techniques[17,15,31]

2. Region growing[18,19,3,24]

3. Central-axis analysis[21,14]

4. Mathematical morphology[20,22,23,16]

The technique proposed by Sonka *et al.* uses an anatomic knowledge base describing structural relationships between airways and neighboring pulmonary vessels.[17,15] Initially, 3D seeded region growing is used to identify large airways. The knowledge-based rules are applied to the image on a slice-by-slice basis. This process results in three types of trees having varying levels of false-positive regions. A fuzzy logic approach was later added by Park *et al.* to improve specificity.[31] The method was not tested on human data. More robust (less knowledge dependent) methods exist.

Region growing methods depend on thresholds to continually grow from a seed point and connect voxels, usually through 26 connectivity.[3,19,18,24] Summers *et al.* use 3D seeded region growing and a manually selected threshold to segment airways for rendering.[3] The algorithm proposed by Mori *et al.* uses an adaptive 3D region growing algorithm that automatically determines a threshold through repeated segmentations.[19] Wood *et al.* also employ 26-connected region growing in conjunction with a global threshold as a basis for airway segmentation.[18] Heng uses adaptive 3D region growing, but adds a genetic algorithm to automatically identify the center of the trachea.[24] Although 3D region growing is efficient, it suffers from partial volume effects and noise due to the global threshold used during segmentation. "Optimal" thresholds differ for large versus small airways because of these factors. The resultant segmentation tends to lack finer details of the airways and contains rough edges. All of these similar methods can either lose details, depict incomplete structures, or suffer from parenchymal leakage ("explosion") to varying degrees.

Segmentation algorithms based on central axis analysis depend on central axis estimates in order to compute the segmentation.[21,14] The segmentation technique proposed by Swift *et al.* performs a central axis computation as a basis for airway segmentation.[21,14] The axis computation begins with a manually selected root site. The surface of an ellipsoid positioned at this site is then sampled to determine more sites or to detect the end of a branch. The properties of the site determine the size of this ellipsoid. This process is then repeated for each newly found site. Further processing produces a complete central axis tree. Bronchial walls are then detected for each site of this tree via thresholding. Finally, the unified results of this process determine the segmented airway tree. The disadvantage to this method is the critical dependence on the central axis analysis results, which may be imperfect or fail for several reasons. Concerns include complex dependencies of initial parameters and stopping criteria, and the possibility of forming paths outside of the airways.

The field of mathematical morphology involves image-processing operations that focus on shape and gray-scale properties.[32,33] Airway segmentation methods drawing upon mathematical morphology tend to have two or more processing phases.[16,20,22,23] First, candidate airways are detected using various morphological operations. Next, 3D relationships and shape characteristics help determine the true airways from false candidates. Bilgen *et al.* proposed an algorithm based on binary and gray-scale morphological operations.[16] 2D operators of varying sizes are applied to each slice of the image to identify candidate airways. Next, false candidates are eliminated by 3D reconstruction. Pisupati *et al.* proposed a similar technique that uses the same principles to detect both pulmonary arteries and veins.[20] Preteux *et al.* use a method based on a combination of morphological filtering, connection cost-based marking, and conditional watershed techniques to segment the bronchi of sheep lungs.[22] 3D tree reconstruction was not considered since the primary focus was 2D airways detection. Extending this work to 3D airway segmentation and reconstruction, Fetita *et al.* have proposed methods that use more complex morphological operations in addition to fractal analysis of candidate regions.[23] An updated selective marking and

depth-constrained connection cost operator is used to identify possible airways. Valid candidates are identified by a 3D reconstruction procedure involving model-based aggregation and fractal analysis. While these methods are promising, computation time tends to be inordinate, particularly for real clinical scenarios. Variations in the properties of the morphological operators directly affect the candidates determined. In addition, the reconstruction process, once candidates are defined, can be complex and unestablished. Further, they have received little or no testing on large high-resolution 3D CT chest volumes.

We present a method that combines the concepts of adaptive 3D region growing and mathematical morphology to give a fast, robust method for 3D airway tree segmentation from very large 3D CT chest images. The remainder of the paper is organized as follows. Section 2 presents the airway segmentation method. Section 3 discusses filtering and the results on human CT data in comparison to other known methods. Section 3 also discusses the utility for human VB analysis for bronchoscopic planning of peripheral nodule biopsy. Finally, Section 4 offers some concluding remarks.

2. METHODS

This section describes the hybrid segmentation algorithm presented by this paper along with the algorithms comprising its basis. The hybrid algorithm will first be detailed followed by its modified components algorithms. These component algorithms are comprised of lung region definition, adaptive 3D region growing, and morphological based segmentation methods. Figure 1 shows how these component algorithms comprise the hybrid algorithm.

2.1. Hybrid Lung Segmentation Algorithm

A diagram of the hybrid algorithm is shown in Figure 1. The necessary inputs are the 3D CT image of the chest and the location of the proximal end of the trachea, the *root site*. The final output is the segmented image of the airways, I_S.

The original image and root site are used throughout the method in computing this final output. The goal of the method is to provide the same quality of segmentation as an existing technique,[16] but with an order of magnitude reduction in computation time. This speedup is achieved by utilizing a modified version of the adaptive region growing method introduced in [19] as well as by lung region definition. More specifically, we identify the locations of larger airways using a modified 3D region growing algorithm. Computationally expensive morphological operators for large airways are then applied only to these identified regions. Areas of the lungs are masked using lung region definition. Operators for smaller airways are applied in the restricted region encompassing only this area. These operators are characterized by their integer size, b. Several other segmentation approaches make use of morphological operations followed by reconstruction.[20,22,23] These approaches can be made more efficient as well with the method introduced. The following paragraphs detail the steps shown in Figure 1.

Lung region definition creates a 3D mask of the data that defines the subvolume of the image containing the lungs. Once the lung region is segmented, the maximum bounding 3D parallelopiped of the segmentation, W_L, is used as a mask for smaller morphological operators, $b = 1, \ldots, s$. Subsection 2.4 describes how these operators of smaller sizes are applied on a slice by slice basis.

Adaptive 3D region growing uses an optional filter along with a manually supplied "explosion" parameter, E, to provide a segmentation of the airways, I_R. The E parameter simply ensures an acceptable volume is segmented. This segmentation is used to provide a set of more refined masks for each slice of the image, $W_R^i, i = 1, \ldots, Z_{size}$. These masks are then used by the remaining larger operators, $b = s + 1, \ldots, M$. Although adaptive 3D region growing is fast, the segmentation does not always capture finer details on the order of one or two voxels in diameter. The resultant segmentation does, however, give an excellent estimate of the location of larger airways. The computation time of this segmentation is insignificant in comparison to any method employing morphological operations. In summary, 3D region growing is used to create a rough segmented volume of the airways, I_R. For each slice $i \in I_R$, a maximum bounding 2D region encompassing the segmented airways, W_R^i, is determined. Each window is then dilated by the radius of the largest operator to ensure proper detection of large airways on the boundaries.

Once the masks, W_L and W_R, are computed, the reconstruction proceeds using the gray scale reconstruction method described in Subsection 2.4. However, the operators are only applied to the regions dictated by these masks.

The hybrid airway segmentation algorithm requires four parameters: 1. E, the explosion parameter for adaptive 3D region growing; 2. s, the maximal operator size considered to be "small"; 3. M, the maximal operator size for morphological operations; 4. T_{MORPH}, the preset threshold used by the morphological operator segmentation
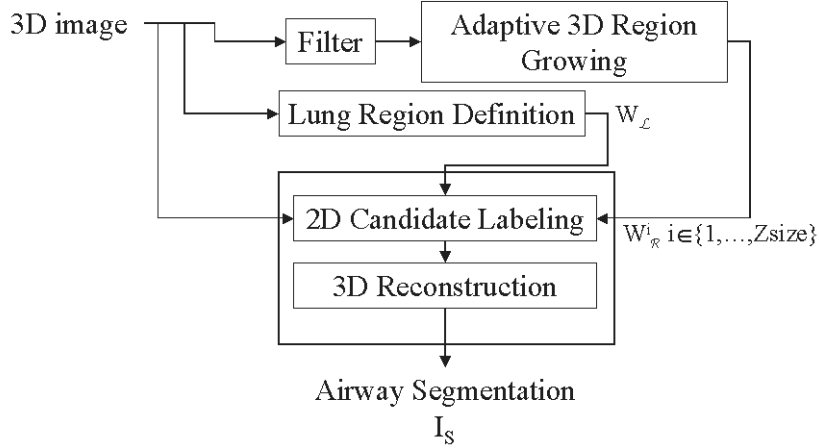
Figure 1. Block diagram of the hybrid airway segmentation algorithm. Lung segmentation and airway segmentation are first performed to produce the regions W_L and W_R^i, respectively. These regions are used to limit the computation time spent by morphological operators in the morphological algorithm.

method. The details of the lung region definition and the adaptive 3D region growing methods along with the morphological approach are found below.

2.2. Lung Region Definition

A partial version of the lung segmentation method by Hu *et al.* is used to identify the lung region.[34] In [34] lung segmentation is performed in three steps to produce separated left and right lungs with smooth boundaries. We used only a portion of the first step since the results of interest need not be precise and are limited to a bounding region for the lungs.

Lung region definition begins with the determination of a threshold to use for region growing at the root site. This threshold is large enough such that the region growing encompasses the entire lungs. The initial threshold, T_0, is set to -1000 HU. An iterative procedure then determines the final threshold. The segmentation threshold at step i, T_i, is used to separate the entire image into voxels greater than T_i and those less than or equal to T_i. The new threshold, T_{i+1}, is set to

$$T_{i+1} = \frac{\mu_b + \mu_n}{2},$$

where μ_b and μ_n represents the mean gray-level of the voxels greater than T_i and that of all other voxels, respectively. This procedure is repeated until the condition $T_i = T_{i+1}$ is met. This threshold is then used for 3D region growing at the root site to define the lung region. 3D region growing is also part of adaptive 3D region growing and is described in the next subsection.

2.3. Adaptive Region Growing

Regions of the image containing larger airways are identified by a robust adaptive 3D region growing method. We increased the robustness of the method in [19] to provide good results for a wide variety of images. The following section first describes adaptive 3D region growing and then describes the modifications made to add robustness.

3D region growing uses a threshold T and a root site (x_r, y_r, z_r) to determine which voxels are added to the segmentation. An optimal T is found by repeating 3D region growing with increasing values of T (adaptive 3D region growing). It is assumed that the threshold eventually reaches a point where it is high enough such that the region growing breaks through the bronchial wall and enters the parenchyma. Since the total volume V of the segmentation is computed each time 3D region growing is performed, this event can be detected by a sharp increase in the volume. The sharp increase is termed an "explosion," and is determined by a preset value called the "explosion parameter," E, that is set to a value below the volume of the explosion. The following paragraphs detail this method.

Let I be the original grayscale image, and let $I_R(x, y, z) = 0, \quad \forall (x, y, z) \in I_R$. I_R will contain the output of the 3D region growing segmentation. Let $N_{26}(x, y, z)$ be the 26-connected neighborhood of the voxel (x, y, z). 3D
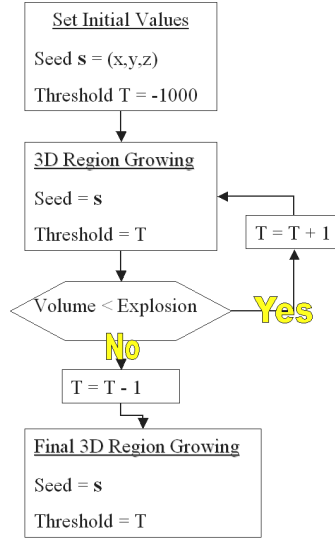
Figure 2. Block diagram of the steps performed in adaptive 3D region growing. The seed s is set to the root site (x_r, y_r, z_r). An optimal threshold is determined as the maximum T that results in a segmentation of acceptable volume. After the optimal threshold T is determined, a final region growing is performed at this threshold.

region growing assumes a threshold T. Given the root site, (x_r, y_r, z_r), each neighbor $(x, y, z) \in N_{26}(x_r, y_r, z_r)$ such that $I(x, y, z) < T$ and $I_R(x, y, z) \neq 1$ is added to the segmentation, i.e., we set $I_R(x, y, z) = 1$. As each voxel is added, its neighbors are then also processed in this fashion. This is repeated until no new voxels are added to I_R. Then, the volume V of this segmentation is computed. The following outlines how repeated 3D region growing operations determine an optimal threshold.

1. Initialize threshold to $T = -1000$ HU.

2. Perform 3D region growing with root site (x_r, y_r, z_r) and threshold T.

3. Calculate the volume of region growing, V, from step 2, i.e.

   $V = \delta x \times \delta y \times \delta z \times \left(\sum_{\forall (x,y,z) \in I_R} I_R(x, y, z) \right)$.

4. If $V \leq E$ repeat step 2 with $T = T + 1$, otherwise continue to step 5.

5. Decrease the threshold, $T = T - 1$. Perform final 3D region growing with this value.

A block diagram of these steps is shown in Figure 2.

There are two modifications we made to adaptive 3D region growing to increase robustness. The first modification is applied to the output segmentation. The final output of 3D region growing is unacceptable in most cases because of cavities in the segmentation due to noise in the original image. Additionally, the region boundaries in the final segmentation are often rough. Solutions to these problems are provided by applying a 2D cavity filling and a 2D binary closing by a 4-connected neighborhood operator to each slice of I_R.[33]

The second modification is the pre-filtering of the data. This option is manually applied on a case-by-case basis. Pre-filtering is necessary when even the minimal initial threshold creates an explosion into the parenchyma. This problem is solved by applying a 2D median filter to each slice.[33] Two different mask sizes are used depending on the severity of the explosion. The first mask is a 4-connected neighborhood and the second is a 3×3 mask. The effects of these filters on region growing are described in the Section 3.

2.4. Morphology-Based Segmentation

In the hybrid method, a modified form of the morphological segmentation method proposed by Bilgen *et al.* accounts for most of the processing.[16] The method of Bilgen *et al.* consists of two steps. First, 2D morphological
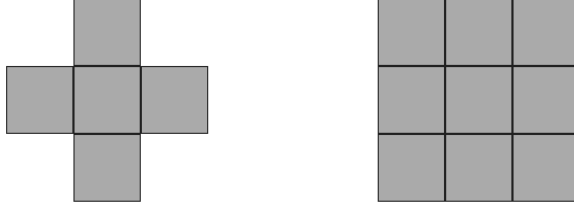
Figure 3. These images are an example of a 4-connected neighborhood operator and a 3×3 operator, respectively.

operations are performed to determine candidate airway locations. This step uses gray-scale reconstruction followed by thresholding applied to each slice. Next, 3D reconstruction is performed to recover the airway tree from these candidate locations. These steps are depicted in Figure 1. The result is a binary segmented volume of the airways, I_S.

Candidate airway locations are determined on a 2D basis via gray-scale reconstruction followed by thresholding. The basis operator for the reconstruction is given by a binary 4-connected neighborhood, B_4, the smallest element used in the process. Figure 3 contains a drawing of this operator. Larger elements are computed by repeated dilations of B_4 as follows:

$$B_4^b = bB_4 = \underbrace{B_4 \oplus B_4 \oplus \ldots \oplus B_4}_{(b-1) \text{ dilations}}, \tag{1}$$

where bB_4 is the bth-order homothetic of B_4.

An operator B_4^b is applied to each individual slice as described below. Given the original image I, each slice $z = 1, \cdots, Z_{size}$ of I is windowed (-1000,0) to a 2D image S,

$$S(x,y) = \begin{cases} I(x,y,z) & \text{if } I(x,y,z) \leq 0 \\ 0 & \text{otherwise} \end{cases}$$

Windowing is used to eliminate the effect of variations in more dense structures such as bone. A marker image for gray-scale reconstruction, J_1, is then obtained from the gray-scale closing of S with structuring element B_4^b,

$$J_1^b = S \bullet B_4^b = (S \oplus B_4^b) \ominus B_4^b. \tag{2}$$

Hence, J_1^b is computed from the gray-scale dilation by B_4^b followed by an erosion by the same operator. Next, J_2^b is computed from J_1^b by the following,

$$J_{k+1}^b = \max(J_k^b \ominus B_4, S), \tag{3}$$

where $\max(.,.)$ computes the voxel-by-voxel gray-level maximum. Equation (3) is repeated until no further changes occur; i.e.,

$$J_\infty^b(x,y) = J_{k+1}^b(x,y) = J_k^b(x,y), \quad \forall (x,y) \in J_k^b, \tag{4}$$

where J_∞^b represents the final gray-scale reconstructed image with structuring element B_4^b. In this image, local minima smaller than B_4^b in S are filled in with a gray-level value that is proportional to the difference between the maximum and minimum gray-levels computed within a B_4^b-sized neighborhood of the minima.

A gray-scale difference image is then computed between J_∞^b and S, and then thresholded,

$$C^b(x,y) = \begin{cases} 1, & \text{if } J_\infty^b(x,y) - S \geq T_{MORPH} \\ 0, & \text{otherwise} \end{cases}$$

The difference image is bright where local minima exist in the image S. We use a value of 20% of the difference between the maximum and minimum possible values for the parameter T_{MORPH}. In this case, since the data was windowed between 0 and -1000, the threshold value is 200. C^b is a binary slice of potential airways identified by operator B_4^b.

In order to identify airways of various sizes, the above process is repeated for each element B_4^b, $b = 1, 2, \ldots, M$, where B_4^M is the maximum sized operator. The union of these series of images is taken to form the final output C for the slice z,

$$C(x, y) = \bigcup_{b=1}^{M} C^b(x, y).$$ (5)

This segmented slice C contains all potential airways acquired through all of the operators. C is then inserted into I_S to define candidate airway locations for slice z,

$$I_S(x, y, z) = C(x, y), \quad \forall (x, y) \in C.$$ (6)

This process is repeated for each slice z of I.

Once the candidate airway locations are in I_S, the 3D airway is reconstructed using a closed space dilation with a unit kernel radius as in [16]. 3D region growing with 6-connectivity, rooted at the trachea, is used in this process. This results in the removal of most false candidates, leaving only the airways in I_S.

Segmentation methods using morphological operations can be computationally expensive. In [16], operators of various sizes are used to detect airways of corresponding sizes. However, these costly operators need not be applied to the entire image, only the approximate location of the airways, since they have no theoretical relevance to other portions of the volume. The hybrid approach uses lung segmentation and adaptive 3D region growing to create masks that greatly constrain the volume where these costly operators are applied.

3. RESULTS

First we discuss the effect of filtering on the robustness of airway segmentation. Next, the performance of the presented algorithm in comparison to two other segmentation algorithms is tested with three 3D CT images. Finally, the utility of the segmentation is demonstrated for human virtual bronchoscopic analysis for a peripheral nodule case.

Three segmentation algorithms were tested and compared: (1) robust adaptive 3D region growing; (2) gray-scale morphological; and (3) hybrid method. 3D CT images obtained from a Philips MX8000 scanner were used in the comparison. The subjects were studied with the University of Iowa IRB approval. The scanning parameters included: 120 kVp, 100 mAs with a multislice pitch of 5 (equivalent to a single pitch of 1.25), 0.5 sec rotation time, 0.6 mm table increment, 180 degrees scan angle, and 1.3 mm slice thickness. An ultra-fast resolution setting with a D filter and a 512 Matrix with a typical field of view of 300-340 mm were used.

The explosion parameter, E, was the only parameter that needed adjustment on a case-by-case basis. We found that settings between 45000 mm^3 and 65000 mm^3 provided acceptable results. The largest operator classified as small, s, is determined by the smallest size airway 3D region growing can continually segment. A value of 3 was used for s since airways with cross sections larger than B_4^3 are hardly influenced by partial volume effects. M, the maximal sized operator is determined from the largest airway in the image. We found that setting $M = 18$ adequately captures all of the airways in our data sets. The following details the effects of filtering on the three algorithms and compares their resultant segmentations.

Filtering the image before segmenting increases the robustness of the algorithms by helping to eliminate voxels of low HU value connecting the airways to the parenchyma. The filtering effects are observed for each of the three algorithms. In some cases, filtering is necessary for successful segmentation.

Figure 4 shows a comparison of the maximum intensity projection, MIP, of the three segmentation algorithms as filtering is added. The filtering has very predictable effects on the region growing segmentation. Looking at the column occupied by the region growing method, as the filtering is increased, there are two noticeable effects. The first effect is a successful segmentation. The second effect is negative in that smaller branches are eliminated in the process. These results are typical for the region growing algorithm.

The hybrid and morphological methods do not respond as predictably to filtering. This behavior is due to the more complex two step process used in computing the segmentation. Filtering has a less predictable effect on the morphological operations, but can still result in improvements in some cases. As shown in Figure 4, the hybrid method improves with filtering. However, the original morphology method identifies additional, non-airway areas when filtering is applied.

In summary, filtering increases the robustness of these algorithms, but comes at a cost of losing smaller branches or identifying additional non-airway structures. Several of the images could not be segmented during the region
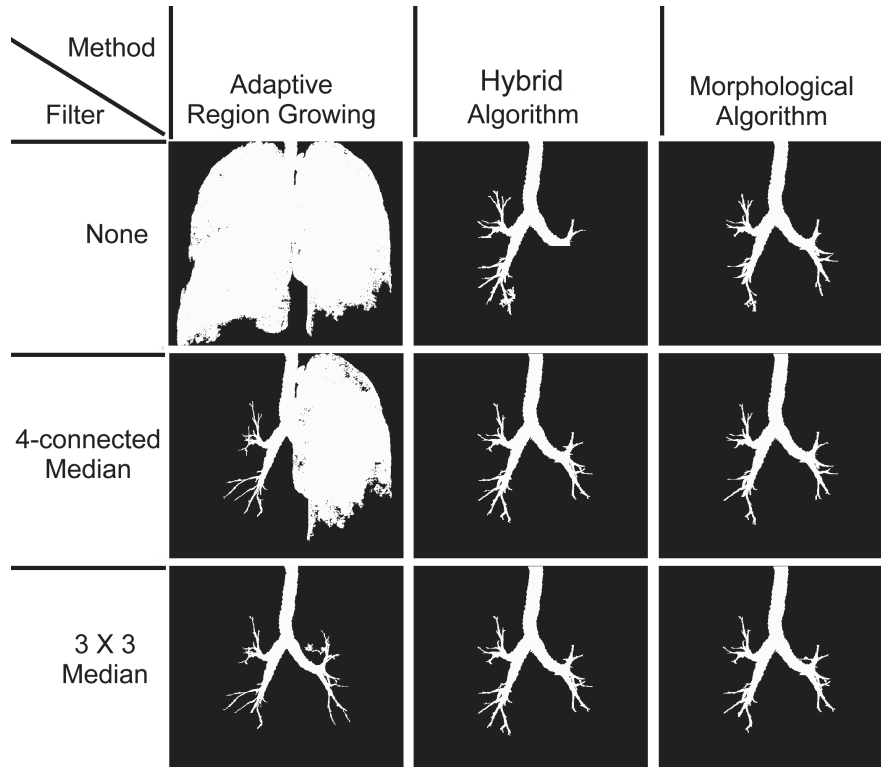
Figure 4. The maximum intensity projection image of different segmentations is shown. The results of three different segmentation algorithms are shown in the columns, while different levels of filters are shown in the rows. Filtering the image before processing increases the robustness of the segmentation methods. However, filtering does remove smaller branches or identifies non-airway regions depending upon the algorithm used.

growing phase of the hybrid algorithm. In all of these cases, the problem was solved by applying a median filter to the image before performing 3D region growing. The 4-connected neighborhood median filter eliminates the finer branches while the 3×3 median filter eliminates even thicker branches. Without this pre-filtering, however, the 3D seeded region growing is unable to segment the airways.

Adaptive 3D region growing, morphological reconstruction, and the hybrid method are compared using the data sets described above. In the following comparisons, two main factors are analyzed, robustness and execution time. Robustness was determined by the capability of the method of completing a visually acceptable segmentation. Execution times excluded image load/save times. Further work will assess these properties more conclusively. Computation times were determined on a 933 Mhz dual-CPU Xeon PIII PC with 2 GB of memory. The final segmented output is currently used in a path planning algorithm to provide smooth navigational paths through the airways

Figures 5, 7, and 8 show the maximum intensity projection (MIP) views of the segmented airways using the three methods. Figure 6 shows the surface rendering of an airway that was computed using the segmentation in the center of Figure 5. Table 1 lists the corresponding timing results for the three different images.

In Figure 5 filtering was not used in any method. The 3D region growing and hybrid methods show similar results. Both methods missed airways recovered by the other. The region growing method experienced a minor explosion in the segmentation. Filtering or lowering the explosion parameter can solve this flaw. However, since the volume of the explosion is small, it would be difficult to determine the proper setting based on the volume increments. The morphological method required approximately 12 times the computation time to perform labeling and failed. The fact that large operators are not applied to the entire image prevented the hybrid method from failing as did the morphological method. Figure 6 displays a surface shaded view of the same airway tree.
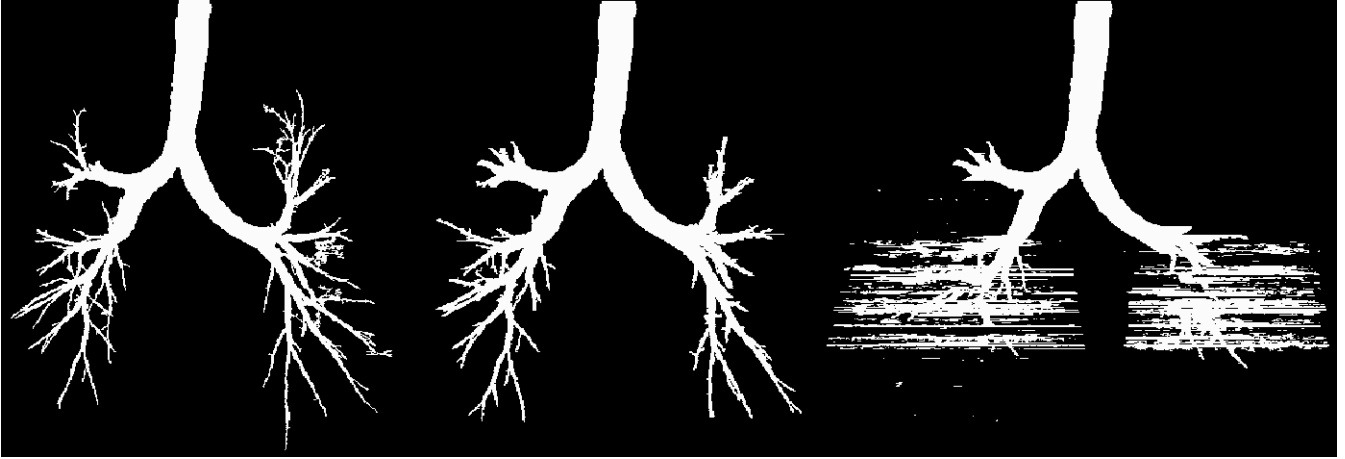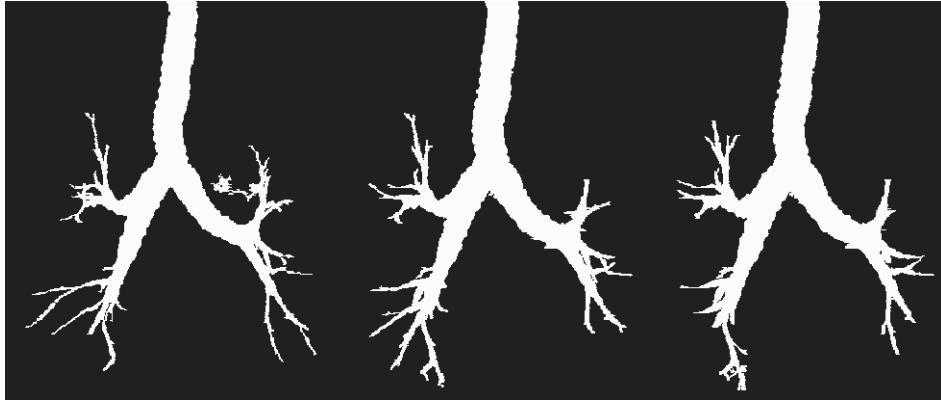
Figure 5. Maximum intensity projections of three different segmentation algorithms for a $512 \times 512 \times 574$ CT image of the chest. The voxel spacing is $\Delta x = \Delta y = 0.724609$ mm, $\Delta z = 0.599976$ mm and the image size is 287 MB. The left image is the result of adaptive 3D region growing. The center image displays the results of the hybrid algorithm. Finally, the right image is from the standard morphological algorithm. All three images were computed without filtering.
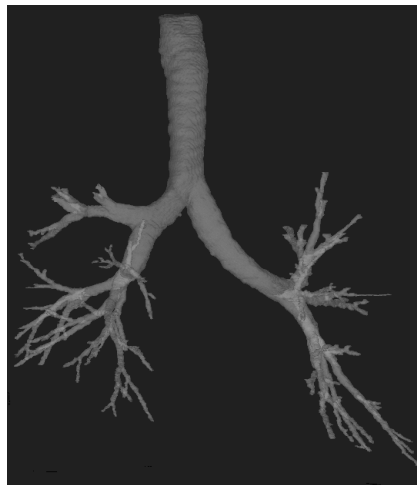

Figure 6. Surface rendering of an airway tree. The segmented image, shown in Figure 5, was used to mask the original gray-scale data. The marching cubes algorithm with a threshold of -600 HU was then applied to the masked gray-scale data to create this surface. This method provides good results for external renderings.

A 4-connected median filter was used for all three methods in Figure 7. All three displayed comparable segmentation quality, but the hybrid method showed no "explosion" artifacts. The labeling time was over 13 times faster for the hybrid method.

Figure 8 displays the third dataset run by the three methods without filtering. The hybrid method was the only successful one. Region growing failed due to a low gray-level voxel directly linking the airways to the parenchyma. The mathematical morphology method failed due to larger structuring elements identifying candidates that eventually linked airways to the parenchyma. The increase in the labeling time speed was only about 5 times in this case. The reason for this smaller difference is due to the explosion of the region growing method, causing the identification of a larger area to apply larger operators. Filtering prevents failure in the other two methods.

Figure 7. Maximum intensity projections of three different segmentation algorithms for a $512 \times 512 \times 488$ CT image of the chest. The voxel spacing is $\Delta x = \Delta y = 0.654297$ mm, $\Delta z = 0.599976$ mm and the image size is 244 MB. The left image is the result of adaptive 3D region growing. The center image displays the results of the hybrid algorithm. Finally, the right image is from the standard morphological algorithm. All three images were filtered with a 2D 4-connected median filter.
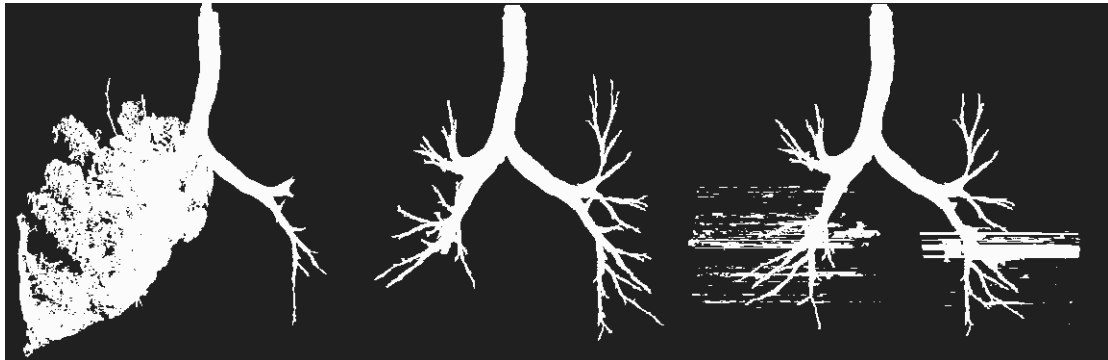
Figure 8. Maximum intensity projections of three different segmentation algorithms for a $512 \times 512 \times 389$ CT image of the chest. The voxel spacing is $\Delta x = \Delta y = 0.585938$ mm, $\Delta z = 0.599976$ mm and the image size is 194 MB. The left image is the result of adaptive 3D region growing. The center image displays the results of the hybrid algorithm. Finally, the right image is from the standard morphological algorithm (failed). All three images were computed without filtering.

Image	Method	Labeling (sec)	Reconstruction (sec)	Total (sec)
1	Adapt. 3D RG	N.A.	N.A.	26
1	Hybrid	1740	2640	4380
1	Standard	21120	4740	25860
2	Adapt. 3D RG	N.A.	N.A.	136
2	Hybrid	960	1020	1980
2	Standard	13200	1320	14520
3	Adapt. 3D RG	N.A.	N.A.	31
3	Hybrid	2400	1080	3480
3	Standard	11820	3540	15360

Table 1. Timing comparisons among three different airway segmentation methods on three different 3D CT images. Time is measured in seconds. Since labeling and reconstruction procedures are not part of adaptive 3D region growing (3D RG), timing results are not applicable (N.A.) for this method. The hybrid method shows approximately an order of magnitude improvement in time for the labeling process.

The hybrid method tends to be more robust than the original method or the region growing method when filtering is not an option. Filtering increases the robustness of all three segmentation methods, but comes at the cost of missing small branches. A more detailed validation study is in progress.

We have applied the segmentation methodology to over 20 human cases thus far, using an integrated virtual bronchoscopy system.[10,35,36,14] The system permits 3D CT image assessment and follow-on live guidance of bronchoscopy. Reference [36] illustrates the system's use for phantom studies, while reference [14] gives preliminary efforts for 3D CT human image assessment.

Figures 9 and 10 illustrate the use of our segmentation methodology and the VB system for a peripheral nodule case. The initial 3D CT image was made on a Marconi Mx8000 multidetector helical CT scanner. It consists of 414 512×512 slices. The slice thickness is 0.6 mm and the axial-plane resolution is 0.566 mm. Figure 9 illustrates airway-tree segmentation results with and without filtering. After segmentation, we computed the centerline paths for the segmented tree using an automated algorithm.[37] Twelve generations of airway branches were extracted, which include 182 branches and 93 paths (see [14] for a definition of a branch and a path); some of the paths toward the periphery are false. The segmentation step took 2 minutes and 26 seconds, while the path analysis required 3 minutes 19 seconds. All processing was done on a Dell Inspiron 3800 laptop (700MHz CPU, 512 MBytes RAM).

Figure 10 gives a composite VB system view for the case. A peripheral nodule is clearly visible in the Coronal Projection view in the right lung. We manually defined the nodule using the system's built-in editing tools. We then created a surface file using a custom surface-dilation procedure and a marching cubes algorithm built into the VTK package.[38] All tools clearly show the nodule, while the Endoluminal Renderer shows an interior view in the right main bronchus. These data can be used conceivably for planning follow-on biopsy.

4. DISCUSSION

We have presented a method to significantly reduce the execution time of morphology-based segmentation algorithms and applied this method to a specific algorithm. Existing segmentation algorithms used in the process were modified to increase robustness through the use of filters. The presented method along with the two segmentation algorithms comprising it were compared using human 3D CT data of the chest.

The results show that no single method is superior in all respects. The morphological method found different airways missed by region growing and had good airway edge localization, but the total run time impractical for clinical usage. Adaptive 3D region growing proves to be the fastest method in obtaining an airway segmentation, but several airways can be missed and the lumen edge definition tends to be poor. The hybrid algorithm significantly reduced the time required for segmentation, allowing practical usage. This method provides good edge localization and produced results similar to the morphological method. The differences in the output between the hybrid and morphological methods are mainly due to the reconstruction process. Since the morphological method identifies more candidates with the larger operators, it is more likely to generate false candidates that create problems for the reconstruction process. Again, the larger operators have no theoretical relevance in locations where there are

(a) No filtering.　　　　　　　　　　　　　(b) star median filter used
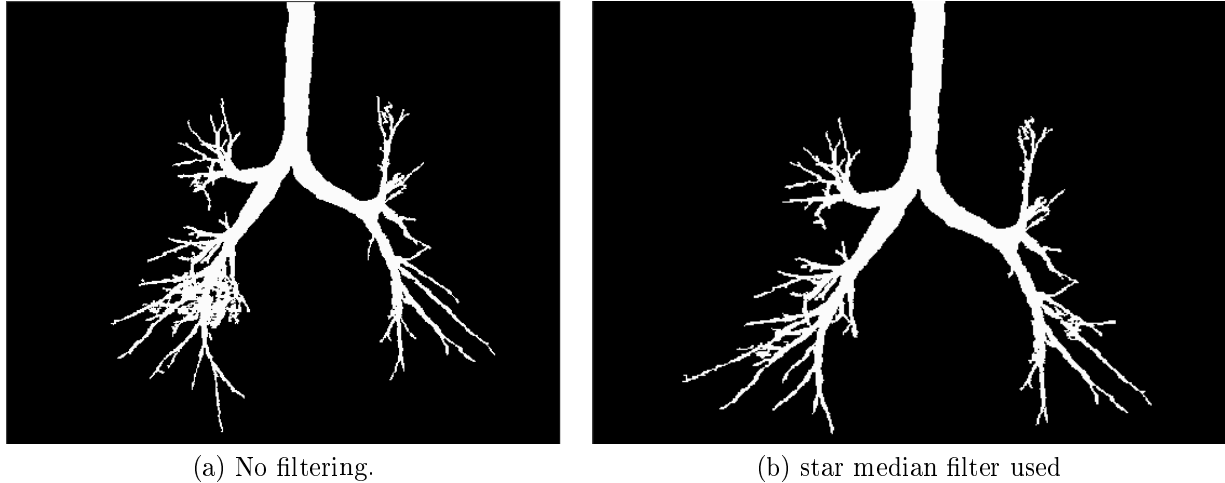
Figure 9. Coronal maximum-intensity projection images of a segmented airway tree for a peripheral nodule human 3D CT scan. See text for image details. Part (a) employs region growing and no filtering [root site = (273,292,0); explosion = 30000] – note the extraneous noisy extensions. Part (b) uses the same segmentation parameters as in part (a), but employs a star median (5-point window, including the four-neighbors of the center point) – the view is significantly cleaner.

no similarly sized airways.

Based on these results, adaptive 3D region growing is appropriate when a fast segmentation is needed for path planning. The hybrid approach offers more in terms of having better edge localization at the cost of more computation time. However, this time is under one hour.

Although it is a manual decision, the use of the median filter before segmentation increases the robustness of all three algorithms. Adaptive region growing benefits the most from this option since the method is prone to having the region growing leak into the parenchyma. This filter reduces the number of connections between airways and the parenchyma.

The presented method is being used as part of a virtual bronchoscopy analysis system to guide path selection and treatment planning.[10] The ability to segment the airways offers a basis for variety of image analysis methods. Path calculations, rendering, and quantitative analysis methods all rely on this segmentation for proper execution. Peripheral nodule guidance is also performed with the segmentation results as a basis.

REFERENCES

1. E. A. Kazerooni, "High resolution CT of the lungs," *American Journal of Roentgenology* , pp. 501–519, Sept. 2001.
2. G. D. Rubin, C. F. Beaulieu, V. Argiro, H. Ringl, A. M. Norbash, J. F. Feller, M. D. Dake, S. Napel, R. B. Jeffrey, and S. Napel, "Perspective volume rendering of CT and MR images: applications for endoscopic imaging," *Radiology* **199**, pp. 321–330, May 1996.
3. R. M. Summers, D. H. Feng, S. M. Holland, M. C. Sneller, and J. H. Shelhamer, "Virtual bronchoscopy: segmentation method for real-time display," *Radiology* **200**, pp. 857–862, Sept. 1996.
4. R. M. Summers, "Image gallery: a tool for rapid endobronchial lesion detection and display using virtual bronchoscopy," *J. Digital Imaging* **11**, pp. 53–55, August 1998.
5. K. H. Englmeier, M. Haubner, C. Kraplicher, D. Schuhmann, M. Seemann, H. Furst, and M. Reiser, "Virtual bronchoscopy based on spiral-CT images," *SPIE Medical Imaging '98: Image Display* **3335**, pp. 427–438, 1999.
6. E. Konin, M. Katz, J. Rozenman, A. Ben-Shlush, Y. Itzchak, and A. Szeinberg, "Virtual bronchoscopy in children: early clinical experience," *Am. J. Roentgen.* **171**, pp. 1699–1702, Dec. 1998.
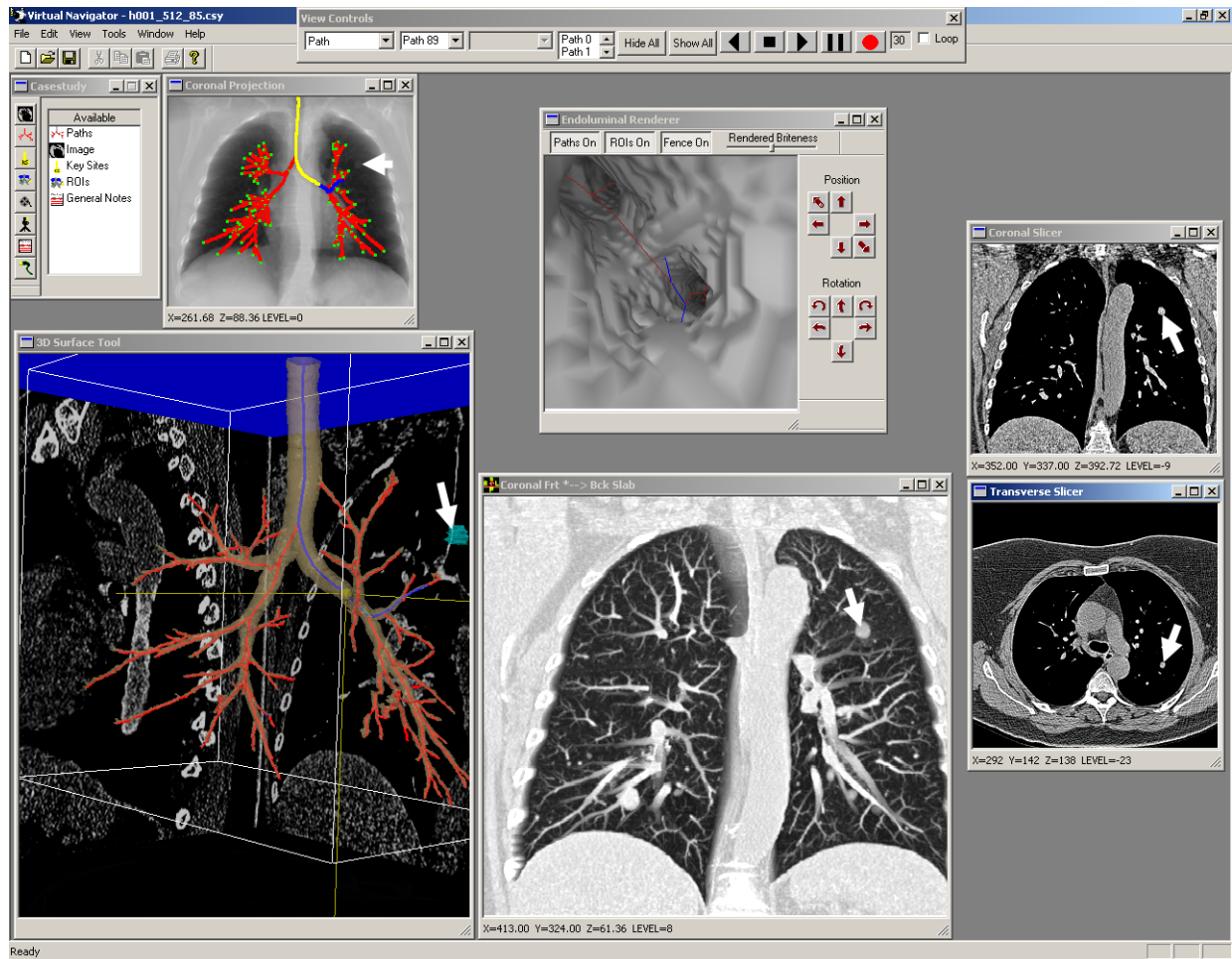
Figure 10. Composite view in a virtual bronchoscopy system for the peripheral nodule case considered in Figure 9. The 3D Surface Tool shows the rendered airway tree and precomputed airway centerlines. One path is highlighted that leads closest to a peripheral nodule. Arrows on the various tools indicate the location of the nodule. The Coronal Projection view is a half-sized maximum-intensity projection of all data between $Y = 150$ and $Y = 400$. It shows the nodule and the highlighted (white) path that is closest to it. The Coronal Front-to-Back Slab depicts a depth-weighted maximum view near the nodule (field of view = 30, depth of vision = 40, viewing window: [-1024,196]).[39] The Transverse and Coronal Slicer views show original slice data in the transverse and coronal directions; mediastinal viewing window used [WL=-40,WW=400]. Finally, the Endoluminal Renderer shows an interior airway view approaching the end of the right main bronchus; this site is shown by the ball in the 3D Surface View and by the termination of the white path in the Coronal Projection view.

7. W. E. Higgins, K. Ramaswamy, R. Swift, G. McLennan, and E. A. Hoffman, "Virtual bronchoscopy for 3D pulmonary image assessment: State of the art and future needs," *Radiographics* **18**, pp. 761–778, May-June 1998.

8. E. F. Haponik, S. L. Aquino, and D. J. Vining, "Virtual bronchoscopy," *Clinics in Chest Med.* **20**, pp. 201–217, March 1999.

9. S. L. Aquino and D. J. Vining, "Virtual bronchoscopy," *Clinics in Chest Med.* **20**, pp. 725–730, Dec. 1999.

10. A. J. Sherbondy, A. P. Kiraly, A. L. Austin, J. P. Helferty, S. Wan, J. Z. Turlington, E. A. Hoffman, G. McLennan, and W. E. Higgins, "Virtual bronchoscopic approach for combining 3D CT and endoscopic video," *SPIE Medical Imaging 2000: Physiology and Function from Multidimensional Images, A. Clough and C.T. Chen, eds.* **3978**, pp. 104–116, Feb. 12-17, 2000.

11. K. Mori, J. Hasegawa, Y. Suenaga, and J. Toriwaki, "Automated anatomical labeling of the bronchial branch and its application to the virtual bronchoscopy system," *IEEE Trans. Medical Imaging* **19**, pp. 103–114, Feb. 2000.

12. C. Pisupati, L. Wolff, W. Mitzner, and E. Zerhouni, "Tracking 3-D pulmonary tree structure," *Proceedings of the IEEE Workshop on Math. Meth. in Biomed. Image Anal., San Francisco, CA* , pp. 160–169, June 1996.

13. V. Sauret, K. A. Goatman, J. S. Fleming, and A. G. Bailey, "Semi-automated tabulation of the 3D topology and morphology of branching networks using CT: application to the airway tree," *Phys. Med. Biol.* **44**, pp. 1625–1638, 1999.

14. R. D. Swift, A. P. Kiraly, A. J. Sherbondy, A. L. Austin, E. A. Hoffman, G. McLennan, and W. E. Higgins, "Automatic axis generation for virtual bronchoscopic assessment of major airway obstructions," *Computerized Medical Imaging and Graphics* , to appear 2001.

15. M. Sonka, W. Park, and E. A. Hoffman, "Rule-based detection of intrathoracic airway trees," *IEEE Trans. Medical Imaging* **15**, pp. 314–326, June 1996.

16. D. Bilgen, E. A. Hoffman, and J. Reinhardt, "Segmentation and analysis of human airway tree from 3D X-Ray CT images," *IEEE Trans. Medical Imaging* , submitted 2001.

17. M. Sonka, W. Park, and E. Hoffman, "Validation of an enhanced knowledge-based method for segmentation and quantitative analysis of intrathoracic airway trees from three-dimensional CT images," *SPIE Med. Imaging '95: Phys. & Func. in Multidim. Images* **2433**, pp. 158–166, 1995.

18. S. Wood, E. Zerhouni, J. Hoford, E. Hoffman, and W. Mitzner, "Measurement of three-dimensional lung tree structures by using computed tomography," *J Applied Physiology* **79**(5), pp. 1687–1697, 1995.

19. K. Mori, J. Hasegawa, J. Toriwaki, H. Anno, and K. Katada, "Recognition of bronchus in three dimensional X-Ray CT images with application to virtualized bronchoscopy system," *Proc. 13th Int. Conf. Pattern Recognition* **III**, pp. 528–532, August 1996.

20. C. Pisupati, L. Wolff, W. Mitzner, and E. Zerhouni, "Segmentation of 3D pulmonary trees using mathematical morphology," *Mathematical Morphology and Its Applications to Image and Signal Processing* , pp. 409–416, May 1996.

21. R. D. Swift, W. E. Higgins, E. A. Hoffman, G. McLennan, and J. M. Reinhardt, "Automatic axis generation for 3D virtual-bronchoscopic assessment," *SPIE Conference on Medical Imaging 1998: Image Processing* **3337, E. Hoffman, ed.**, pp. 73–84, 21-27 Feb. 1998.

22. F. Prêteux, C. Fetita, P. Grenier, and A. Capderou, "Modeling, segmentation and caliber estimation of bronchi in high-resolution computerized tomography," *Journal of Electronic Imaging* **8**, pp. 36–45, January 1999.

23. C. Fetita and F. Prêteux, "Bronchial tree modeling and 3D reconstruction," *Proceedings SPIE Conference on Mathematical Modeling, Estimation and Imaging, San Diego, CA* **4121**, August 2000.

24. T. Y. Law and P. A. Heng, "Automated extraction of bronchus from 3D CT images of lung based on genetic algorithm and 3D region growing," *SPIE Medical Imaging 2000: Image Processing, K.M. Hanson, Ed.,* **3979**, pp. 906–916, 2000.

25. W. Kalender, *Computed Tomography: fundamentals, system technology, image quality, applications*, Publicis MCD Verlag, Munich, 2000.

26. J. M. Reinhardt, N. D. D'Souza, and E. A. Hoffman, "Accurate measurement of intrathoracic airways," *IEEE Trans. Medical Imaging* **16**, pp. 820–827, Dec. 1997.

27. H. S. Choi, D. R. Haynor, and Y. Kim, "Partial volume tissue classification of multichannel magnetic resonance images – a mixel model," *IEEE Transactions on Medical Imaging* **10**, pp. 395–407, Sept 1991.

28. H. Soltanian-Zadeh, J. P. Windham, and A. E. Yagle, "Optimal transformation for correcting partial volume averaging effects in magnetic resonance imaging," *IEEE Trans. on Medical Imaging* **40**, pp. 1204–1212, Aug 1993.

29. P. Santago and H. D. Gage, "Statistical models of partial volume effect," *IEEE Trans. on Image Processing* **4**, pp. 1531–1540, Nov 1995.

30. P. M. Tardif, "Virtual reality in radiology: virtual intervention," *SPIE Medical Imaging 2001: Image Processing, M. Sonka and K.M. Hansen, eds.* **4322**, Feb. 19-22 2001.

31. W. Park, E. A. Hoffman, and M. Sonka, "Segmentation of intrathoratic airway trees: A fuzzy logic approach," *IEEE Trans. Medical Imaging* **17**, pp. 489–497, August 1998.

32. J. Serra, *Image Analysis and Mathematical Morphology*, Academic Press, San Diego, vol. 1, 1988.

33. R. C. Gonzalez and R. E. Woods, *Digital Image Processing*, Addison Wesley, Reading, MA, 1992.

34. S. Hu, E. A. Hoffman, and J. M. Reinhardt, "Automatic lung segmentation for accurate quantitation of volumetric X-Ray CT images," *IEEE Transactions on Medical Imaging* **20**, pp. 490–498, June 2001.

35. J. P. Helferty, A. J. Sherbondy, E. A. Hoffman, G. McLennan, and W. E. Higgins, "Experiments in virtual-endoscopy guidance of bronchoscopy," *SPIE Medical Imaging 2001: Physiology and Function from Multidimensional Images, C. Chen and A. V. Clough, eds.* **4321**, Feb 18-22 2001.

36. J. P. Helferty and W. E. Higgins, "Technique for registering 3D virtual CT images to endoscopic video," *IEEE Int. Conf. Image Processing* **II**, pp. 893–896, Oct. 7-10 2001.

37. A. P. Kiraly and W. E. Higgins, "A general path-planning algorithm for segmented tubular structures," in *in preparation,*

38. W. Schroeder, K. Martin, and B. Lorensen, *The Visualization Toolkit: An Object-Oriented Approach To 3D Graphics*, Prentice Hall, Upper Saddle River, N.J., 1997.
39. J. Z. Turlington and W. E. Higgins, "New techniques for efficient sliding thin-slab volume visualization," *IEEE Trans. Medical Imaging* **20**, pp. 823–835, Aug. 2001.